Scientia Iranica B (2020) 27(4), 1995–2008

Sharif University of Technology
Scientia Iranica
Transactions B: Mechanical Engineering
http://scientiairanica.sharif.edu

Tensile creep monitoring of basalt fiber-reinforced polymer plates via electrical potential change and artificial neural network

W.A. Altabey[a,b,c], **M. Noori**[d,*], **A. Alarjani**[b], **and Y. Zhao**[e]

a. *International Institute for Urban Systems Engineering, Southeast University, Nanjing 210096, China.*
b. *Department of Mechanical Engineering, College of Engineering in Alkharj, Prince Sattam Bin Abdelaziz University, Alkharj 11942, Saudi Arabia.*
c. *Department of Mechanical Engineering, Faculty of Engineering, Alexandria University, Alexandria 21544, Egypt.*
d. *Department of Mechanical Engineering, California Polytechnic State University, San Luis Obispo, California, USA.*
e. *International Institute for Urban Systems Engineering, Southeast University, Nanjing 210096, China.*

Received 29 January 2019; received in revised form 14 October 2019; accepted 1 June 2020

KEYWORDS
Tensile Creep Monitoring (TCM);
Creep time;
Electrical Capacitance Sensor (ECS);
BFRP;
FEM;
ANNs.

Abstract. In this research, Long-Term Tensile Creep (LTTC) failure in Basalt Fiber-Reinforced Polymer (BFRP) composites under ambient conditions was predicted and detected via an expert system in order to monitor the LTTC of BFRP laminated composites. This was accomplished by using a highly accurate, easy to use, and low-cost monitoring method incorporating an Electrical Potential Change (EPC) technique that employs an Electrical Capacitance Sensor (ECS) in conjunction with an Artificial Neural Network (ANN) to improve the process of detecting and predicting LTTC. A Finite Element (FE) simulation model for Tensile Creep (TC) detection was generated by ANSYS to obtain groups of data for the training of ANNs. The proposed method was then applied to minimize the extent of FE analysis in order to reduce the time required for the monitoring of creep behavior to a minimum. First, creep monitoring at different levels of TC (%σc) as a percentage of Ultimate Tensile Strength (UTS) equal to 25%, 50%, and 75% was studied. Subsequently, the trained ANN was utilized to predict the creep behavior at different TC levels (%σc) of 15%, 35%, 60%, and 85%, excluded from the FE data. The results showed excellent agreement between FE and predicted results.

1. Introduction

Basalt fiber is a relatively new and viable alternative material to the more commonly used composite fibers due to its good mechanical properties and lower production cost. For this purpose, as a key measure for assessing the performance and mechanical behavior of Basalt Fiber-Reinforced Polymers (BFRP), creep monitoring is important. It is particularly critical to detect long-term displacement levels and Creep Time (CT) for these new and advanced materials [1–6].

Due to the viscoelastic nature of the polymer matrix, the degradation of the modulus as a function of time, characterized by creep of polymer composites, has become a major concern for making structural parts using a polymer composite. Over the last three decades, considerable research has been conducted to understand the creep behavior of polymer matrices and

*. *Corresponding author. Tel.: +1 805 903 2411*
E-mail addressess: wael.altabey@gmail.com (W.A. Altabey); mnoori@outlook.com (M. Noori); alis.alarjani@gmail.com (A. Alarjani); yzhseu@gmail.com (Y. Zhao)

doi: 10.24200/sci.2020.52754.2874

composite structures. However, these studies on composite materials are very limited and inadequate [7].

According to literature, several techniques have been employed by various researchers to evaluate the mechanical properties of composite materials under creep tests. As reported in nearly all of the related published works, for tensile creep tests at maximum load, 50% of Ultimate Tensile Strength (UTS) has been considered. Researchers have also studied non-linear viscoelastic models for composite materials at different levels of stress between 20 and 60 MPa in the temperature range of up to 90°C [8,9]. According to the findings of the above studies, it can be generally concluded that composite materials exhibit non-linear behavior at all applied levels of stress. In another relevant study on the creep behavior of a carbon/epoxy composite by using tensile and flexural creep testing, it was found that there was no creep rupture failure of the studied composites under a loading up to 77% of UTS for 1600 h at room temperature [10].

It is widely known that the performance and creep behavior of laminated composites are influenced by the properties of the matrix utilized in making the composites. The creep behavior of these composites not only maintains the desired form and protects the reinforcements against external attacks but also has an important role to play in the creep of composites. As discussed in the literature, the characterization of laminates has been studied based on the type and architecture of reinforcements [11] and is based on the epoxy matrix that influences its properties [12,13]. In this context, the creep behavior is strongly influenced by the viscoelastic properties of resin and the characteristics of fibers. In the case of Glass Fiber Reinforced Polymer (GFRP), the creep limit is 0.3UTS; in the case of Carbon Fiber Reinforced Polymer (CFRP) and Aramid Fiber Reinforced Polymer (AFRP), it is the rupture limit to the creep of 0.7UTS according to the recommendations of the American Concrete Institute (ACI) 440.4R04 [14].

Based on this literature review and to the best of the authors' knowledge, it is noted that no studies have investigated BFRP composites and the corresponding creep behavior. Therefore, this paper aims to provide more information on the effect of the creep behavior on the mechanical performance of BFRP laminated composites.

Fiber Reinforced Polymer (FRP) damage detection is complex in general and it is a difficult and expensive task to conduct during an inspection due to creep strain. The detection difficulty indicates the importance of developing an easy and economical technique for monitoring damage due to creep in FRP laminated composites [15–17]. The conventional Non-Destructive Test (NDT) methods, e.g., magnetic particle inspection or ultrasonic inspection techniques, are not able to detect creep damage because these methods are not able to detect damage prior to the formation of a creep crack in composite structures. Moreover, (a) traditional methods of sensing, which utilize strain gauges and vibration-based and piezoelectric type sensors, and (b) innovative monitoring techniques, which use advanced sensors such as optical fibers, generally incorporate sensors inside or outside of the structure and they are commonly expensive [18–25].

In order to overcome these disadvantages, a number of other monitoring systems based on the intrinsically dielectric properties of materials have recently been studied. The methodology presented in this paper entails the measurement of Electrical Potential Change (EPC) of model parts using a row of electrodes mounted on the outer surface of structures without utilizing additional sensors. This row of electrodes measures the capacitance change due to the change in dielectric permittivity. Compared to other techniques such as traditional fiber optic sensors, the advantages of monitoring systems based on dielectric properties for damage detection in composite structures include the higher reliability and lower cost. Moreover, it is not possible to apply an intensive network of fiber optic sensors to large composite structures. Moreover, crack detection will fail if crack propagation does not intersect with the sensors. Furthermore, the installment of fiber optic sensors may result in initiating damage [26,27]. Conversely, Electrical Capacitance Sensor (ECS) offers more advantages such as low cost, fast response, low sensitivity to noise, higher safety, and continued operability under harsh environmental conditions [28–33].

Zhao et al. [34] studied a damage identification system for CFRP composite pipes using a 3D ECS model. They subsequently derived the transfer function of the system and applied it to an 'open-loop' pipeline model using deep learning-based damage identification by extracting modal macro strains from dynamic excitations [35]. The proposed modulation method extended in this paper was tested in our previous work for crack monitoring due to fatigue load in laminated composite pipes [36] for identifying delamination [37,38] and detecting the mechanical properties and strength degradation of Glass Fiber Reinforced Epoxy (GFRE) composite pipes due to water absorption from internal hydrostatic pressure [39]. Altabey et al. [40] monitored the nano-delamination embedded in BFRP nano-pipes of EPC with Artificial Neural Network (ANN) for the first time and found that the proposed technique successfully assessed the nano-delamination embedded in composite nano-pipes within a low error band. In all of the previous works using ECS electrodes, the node potential values were measured before and after damage initiation.

To the best of our knowledge, no paper dealing with the electrical capacitance monitoring of FRPs under creep conditions can be found in the open scientific literature. Therefore, the aim of this work is to investigate the Long-Term Tensile Creep (LTTC) behavior at different levels of TC (%σc) in BFRP laminated composite plates using ECS, whose strain and damage evolution under creep loading conditions is monitored by measuring the capacitance change due to the change in dielectric permittivity. In order to overcome the drawbacks of alternative monitoring systems, an ANN algorithm is utilized in this work to reduce the complexity of detecting and predicting the LTTC. First, the trained ANN is utilized to predict the Finite Element (FE) outcome of LTTC behavior and, then, it is subsequently used to predict the LTTC behavior at different levels of TC (%σc) excluded from the FE data. The results show excellent agreement between FE results and those predicted by ANN.

2. Description of the sensor

ECS was used for the first time in the 1980s by a research group from the US Department of Energy to measure fluidized bed systems [41–43]. Subsequently, the technique has been further developed over the last 10 years. This approach has drawn the attention of the research community and has become significantly applicable to industrial process monitoring due to its low cost and reliable operation under harsh environments. ECS measures the capacitance change of multi-electrode sensors due to the change of dielectric permittivity being imaged and, then, it reconstructs the cross-section images using the measured raw data with a suitable algorithm such as the algorithm used in this work via ANN. Electrical capacitance system includes a sensor and a capacitance measuring circuit, as shown in Figures 1 and 2. ECS consists of an insulating plate, measurement electrodes, and an earthed screen. The measurement electrodes are mounted on the top surface of the plate. The earthed screen is fitted between the electrodes to cut the electro line external to the sensor plate and reduce the inter-electrode capacitance. The earthed screen surrounds the measurement electrodes to shield external electromagnetic noise.

To increase the accuracy of ECS measurements, the factors affecting the sensitivity of ECS and its application domain have been studied. These studies have included the impact of structural material and inner dielectric permittivity [44–52] and the structural geometry (thinness ratio of structures) [53,54]. Altabey [55] studied the effect of environmental temperature on ECS working field for the first time and found that the ECS working field temperature caused substantial changes in the sensitivity of the ECS electrodes as well as its working domain.

2.1. Geometric model

Figure 1 illustrates the LTTC failure monitoring system using the EPC with an ANN system. The model consists of seven electrodes that are fixed on one single side of the specimen surface, as shown in Figure 1. The plate used for the ECS in this research included a square plate with a length of 280 mm and a height of 15 mm. The plate was made of BFRP composite material with a row of seven electrodes that were mounted on a single surface of the plate, separated from each other by a 45 mm gap. Figure 3 illustrates the cross-section of seven electrodes of the ECS system configuration. The capacitance values of each pair of electrodes were measured via ECS, and the equivalent of node potential from the measured capacitance values was converted. The numbering order of electrodes system is shown in Figure 2. In ascending order, the electrodes were excited one by one so that if

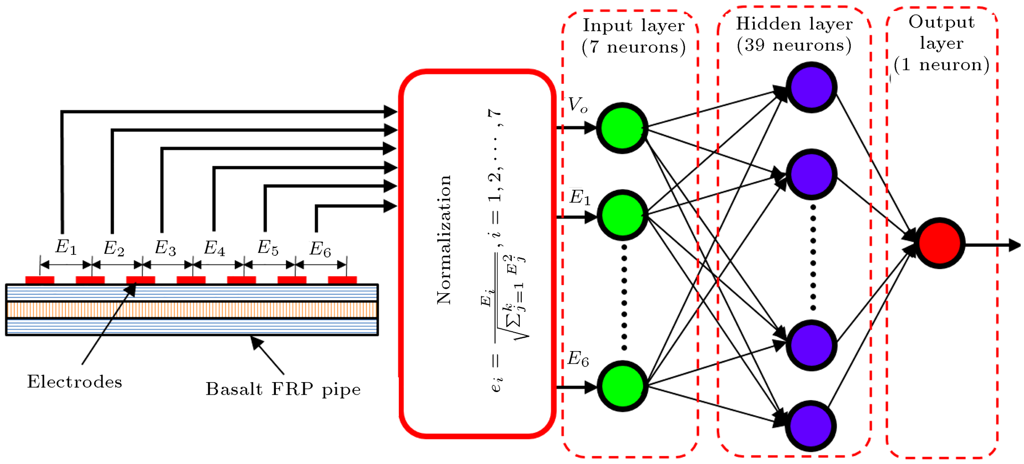

Figure 1. Schematic representation of the monitoring method using Electrical Capacitance Sensor (ECS) and RS methods with an Artificial Neural Network (ANN).

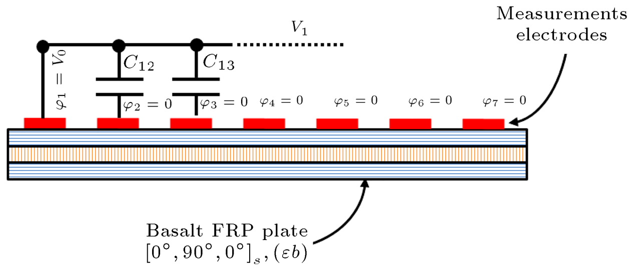

Figure 2. Schematic representation of the measurement principle of an Electrical Capacitance Sensor (ECS).

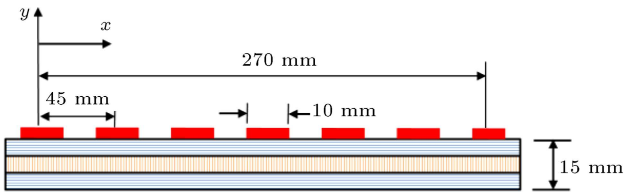

Figure 3. Cross-section sketch of seven electrodes Electrical Capacitance Sensor (ECS).

one electrode was excited, other electrodes would be recorded at ground potential as detector electrodes (see Figure 2). The electrode capacitance, C_{ij}, can be calculated by using these charge measurements from Eq. (1):

$$C_{ij} = \frac{Q_{ij}}{\Delta V_{ij}}, \tag{1}$$

where Q_{ij} is the charge induced on electrode j when electrode i is excited with a known potential. V_{ij} is the potential difference between electrodes i and $j(\Delta V_{ij} = V_i - V_j)$.

Thus, the number of independent capacitance measurements $M = 21$ using Eq. (2) is as follows:

$$M = \frac{N(N-1)}{2}. \tag{2}$$

2.2. FF simulation model

The structural properties of the BFRP laminated composite plate are shown in Table 1. Figure 4 represents the geometric model of the laminated composite plate structure. These BFRP composite properties were tested at the National and Local Joint Engineering Research Center for FRP Production and Application Technology, Nanjing, China, a high-tech company specializing in the research and development, manufacturing, marketing, and technical assessment of high-performance fibers and composites.

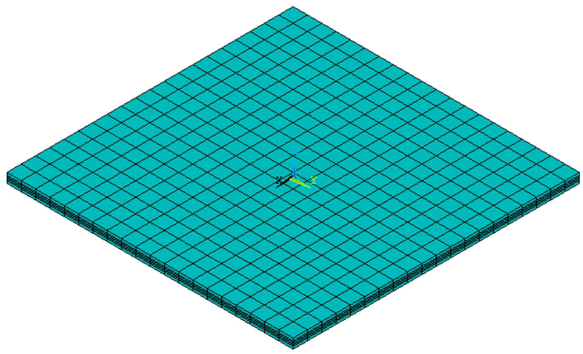

Figure 4. Element map of finite element mesh.

Figure 4 shows that the laminated composite square plate has a length of 280 mm with 15 mm in height and the staking distribution to three plies is $[0/90°/0]_s$. The thickness of each ply is 5 mm.

2.3. ECS Governing equations

The main target of derivations is to compute the capacitance matrix C from sensor parameters and structure material permittivity distribution $\varepsilon(x, y)$; therefore, the first governing equation of ECS is Poisson's equation [34,36–39]:

$$\nabla.\varepsilon(x, y)\nabla\varphi(x, y) = 0. \tag{3}$$

By solving Poisson equation (Eq. (3)) for the terminals Boundary Condition (BC) of ECS measurement system, the potential distribution inside the ECS $\varphi(x, y)$ can be determined.

The other two sensor parameters include the electric field vector $E(x, y)$ and the electric flux density $D(x, y)$ calculated as follows [34,36–39]:

$$E(x, y) = -\nabla\varphi(x, y), \tag{4}$$

$$D = \varepsilon(x, y)E(x, y). \tag{5}$$

Gauss's law is used to find changes in the electrodes and the inter electrode capacitances. The law has been solved based on the following surface integral [34,36–39]:

Table 1. Structural properties of the Basalt Fiber-Reinforced Polymer (BFRP).

Element type	ρ (kg/m^3)	EX (GPa)	EY (GPa)	EZ (GPa)	PRXY	PRYZ	PRXZ	GXY (GPa)	GYZ (GPa)	GXZ (GPa)
PLANE121	2700	96.74	22.55	22.55	0.3	0.6	0.3	10.64	8.73	10.64

Remark: BFRP is Basalt Fiber-Reinforced Polymers, ρ is material density, EX, EY, EZ are elastic moduli in the X, Y, and Z directions, respectively, GXY, GYZ, GXZ are shear moduli in the XY, YZ, and XZ planes, respectively, PRXY, PRYZ, PRXZ are Poisson's coefficients in the XY, YZ, and XZ planes, respectively.

Table 2. Electrical properties.

Element type	Permittivity	PERX ($F.m^{-1}$)	PERY ($F.m^{-1}$)	PERZ ($F.m^{-1}$)	RSVX ($\Omega.m$)	RSVY ($\Omega.m$)	RSVZ ($\Omega.m$)
SOLID123	Water	78.36	78.36	78.36	1E4	1E4	1E4
	Oil	3.0	3.0	3.0	3E11	3E11	3E11
	C_2H_5OH	24.5	24.5	24.5	7.4E6	7.4E6	7.4E6
	BFRP	2.2	1.32	1.32	0.01	0.01	0.01
	Electrode	1E10	1E10	1E10	1.75E-6	1.75E-6	1.75E-6
	Air	1.0	1.0	1.0	3E13	3E13	3E13

Remark: Other parameters of the electrical property can be found in [60–62].

$$Q_{ij} = \oint_{S_j} (\varepsilon(x,y)\nabla\varphi(x,y).\hat{n})dS, \tag{6}$$

where $(\nabla.)$ is the divergence, (∇) is the gradient of parameters, S_j is a surface enclosing electrode $j, \hat{n}$ is the unit vector normal to S_j and infinitesimal area dS on electrode.

2.4. The FE model description

To investigate the effect of TC on the dielectric properties of the BFRP laminated panel, the FE analysis of the electric field intensity of laminated panel was designed using ANSYS ver.15 [56–59]. Suitable FEs were selected and employed to simulate BFRP properties, i.e., PLANE121 element is used to simulate structural property and SOLID123 is used to simulate electrical property. The elements were of rectangular 4-node type. Nodes and elements at each ply are 441 and 400 in number, respectively. The mesh size is 14 mm, the panel has fixed structural BCs on the one side, the tensile load is applied to the opposite side, and the other two sides are free. In electrical BCs, elements at each node have one degree of freedom (voltage). Tables 1 and 2 list all of the parameters required for multi-physics coupled field analysis. Other parameters of the electrical property can be found in [60–62]. The outcome of ANSYS software is the potential and electric field values (see Eq. (4)) at the element nodes. For each electrode, the potential BC is $V_0 = 15$ V (RMS) applied one by one, such that one electrode is excited with 15 V (RMS) and other electrodes are kept at ground ($V = 0$) potential. To represent the natural propagation of electric field, the default BC of continuity ($\hat{n} \cdot (D_1 - D_2) = 0$) was maintained for the internal boundaries.

3. Description of the ANN algorithm

ANNs were used and developed first in the 1940s as information processing for non-linear and complex systems. Subsequently, the approach has been developed quickly over the last two decades and the approach has found a wide range of practical applications in numerous fields of engineering. One of the targets of ANN is to find complex and non-linear relationships between the input and output that cannot be found directly from experimental or numerical data. This is carried out by the proper training of ANN. Several types of ANN architectures have been used in different applications with different algorithms [63]. In this study, the ANN was applied to predict the electric potential differences between ECS electrode pairs.

3.1. ANN configuration

Due to several ANN configurations and the effects of these configurations on predictive accuracy and quality, it is necessary to describe the ANN configuration using a simple and easy code; this study used a general ANN configuration algorithm as follows:

$$\{N_{in}[N_{h1}N_{h2}]_e N_{out}\} \equiv \left\{7\left[39 \quad 2\right]_2 1\right\}, \tag{7}$$

where N_{in} and N_{out} are the element numbers of input and output parameters equal to 7 and 1, respectively, and e is the number of hidden layers equal to 2. N_{h1} and N_{h2} are numbers of neurons in each hidden layer equal to 39 and 2, respectively.

Note that the effectiveness of ANN depends on the related interconnections that increase based on the number of neurons in each hidden layer. These interconnections also represent the relationship between input and output. Thus, more training datasets are required to learn these relationships.

This study also needs to optimize the number of neurons in each hidden layer in ANN architecture [64].

3.2. Feed-Forward Neural Networks (FFNN)

FFNN is the most commonly used ANs architecture type. It consists of a layer of input, a layer of output, and one or more hidden layers of neurons for full interconnection between input and output layers [65]. The hidden and output layer neurons use nonlinear activation functions such as linear transfer function (*purelin (n)*), Tan-Sigmoid transfer function (*tansig (n)*), or Radial Basis (Gaussian) transfer functions (*radbas (n)*). However, no activation function is used in the input layer since no computation is involved in that layer, and the data flows between layers in a feed-forward manner.

The training of FFNN continues until the Mean-Square-Error (MSE) between the input data and the network outcomes has reached a suitable value or after the completion of a pre-specified number of learning epochs. The MSE can be computed through the following equation:

$$MSE = \sum \left((E_{i-j})_{nn} - E_{i-j} \right)^2 / 2, \tag{8}$$

where $(E_{i-j})_{nn}$ is the predicted electric potential differences, E_{i-j} is the electric potential differences measured using the FE method, and n is the number of the FE measured data values.

4. Results and discussion

4.1. Experimental validation

The experimental dataset used in this work to validate the proposed technique was adapted from Goertzen and Kessler [66]. The tests were conducted on composite laminated panels that were prepared with 2 plies of bidirectional woven Carbon Fiber-Reinforcement Epoxy (CFRE). Composite panels had the dimensions of 12 in×10 in (304.8 mm × 254 mm). The composite fiber volume fraction (V_f) was measured to be between 35% and 40%. The thickness of the creep rupture specimens ranged from 1.1 to 1.2 in (27.94 to 30.48 mm). TC testing was performed using an in-situ creep rupture fixture (see Figure 5) developed by Lombart [67] at the University of Tulsa. Goertzen and Kessler [66] conducted the Tensile Creep Compliance (TCC) $S(t) = 1/E(t) = \varepsilon(t)/\sigma(t)$ for the test specimens at 417 MPa (60.5 ksi) (65% UTS) and 496 MPa (72.0 ksi) (77% UTS).

To conduct a convergence investigation of the proposed technique, seven electrodes were fixed on the single side of the laminated panel surface with the same geometrical specifications. For the electrode model, the thickness of electrodes was 10 mm, the space between electrodes was 45 mm, and the BC of ECS was ($V = V_0$) with +15 V (V_0). The EPC between electrode pairs was measured in various cases of TC ($\%\sigma_c$) as the percentage of UTS and was compared with the experimental results of Goertzen and Kessler [66].

Figure 6 shows the comparison between finite element data of the TCC ($S(t)$) and experimental data by Goertzen and Kessler [66] for the same laminated panel geometrical specifications, initial conditions, and CT.

From Figure 6, one can see excellent convergence between the FE and experimental data of the TCC ($S(t)$) with an average error of 2.2%. A small variation between the experimental and FE data exists because the finite element simulations ignore the fringe-field effects at the outer edges of the electrodes.

4.2. EPC technique for TCM

Seven electrodes were mounted on a single side of the specimen surface. For the electrode model, the

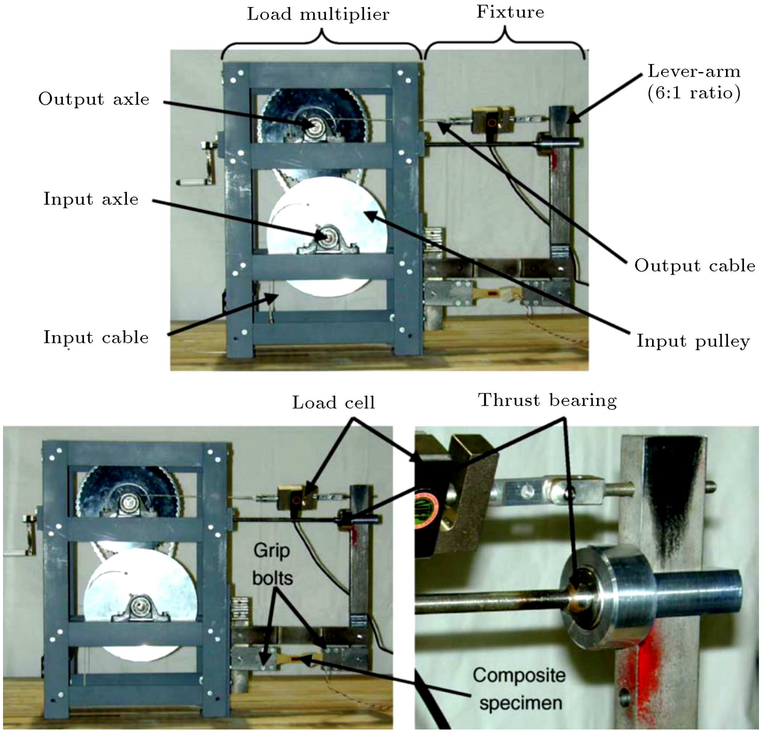

Figure 5. In-situ creep rupture fixture [67].

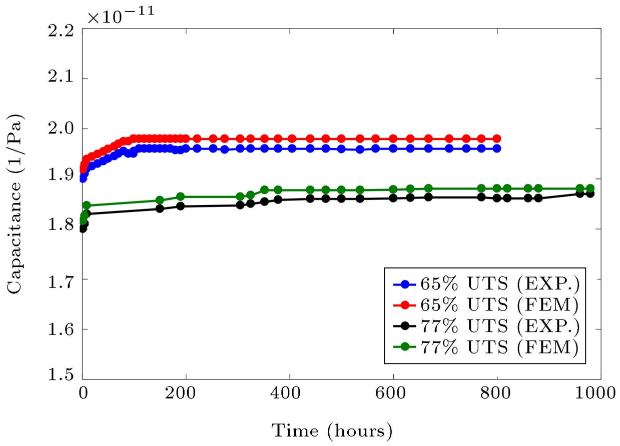

Figure 6. Comparison between Finite Element (FE) data of the Tensil Creep Comliance (TCC) ($S(t)$) and experimental data by Goertzen and Kessler [66].

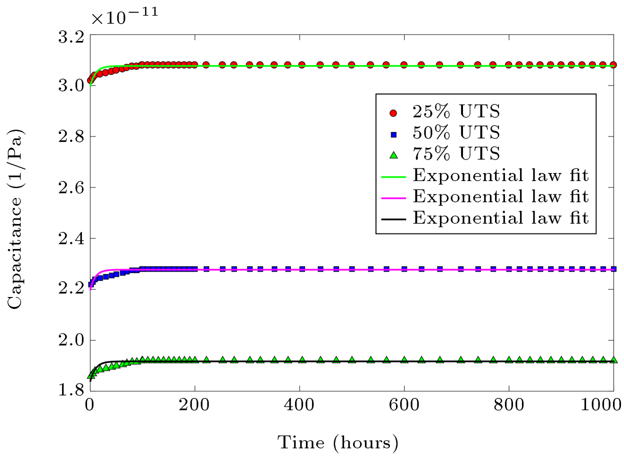

Figure 7. Tensil Creep Comliance (TCC) ($S(t)$) of Basalt Fiber-Reinforced Polymer (BFRP) vs. Creep Time (CT), Tensile Creep (TC) ($\%\sigma_c$)= 25%, 50%, and 75% Ultimate Tensile Strength (UTS).

thickness of electrodes was 10 mm, the space between electrodes was 45 mm, and the BC of EP was ($V = V_0$) with +15 V (V_0). The EPCs between electrode pairs were measured in various cases of TC ($\%\sigma_c$) percentage of UTS equal to (25%, 50%, and 75%). From the measured data, TCC ($S(t)$) for each TC ($\%\sigma_c$) percentage was obtained using the scripting capabilities in ANSYS.

Figure 7 shows the TCC, $S(t) = 1/E(t) = \varepsilon(t)/\sigma(t)$, for the BFRP Plate conducted at 135 MPa (25% UTS), 270 MPa (50% UTS), and 405 MPa (75% UTS).

According to Figure 7, it can be found that the compliance values of 25% UTS simulation were larger than those of 50% and 75% UTS simulation. This difference between compliance values resulted from fluctuations in the modulus of the composite material over the CT.

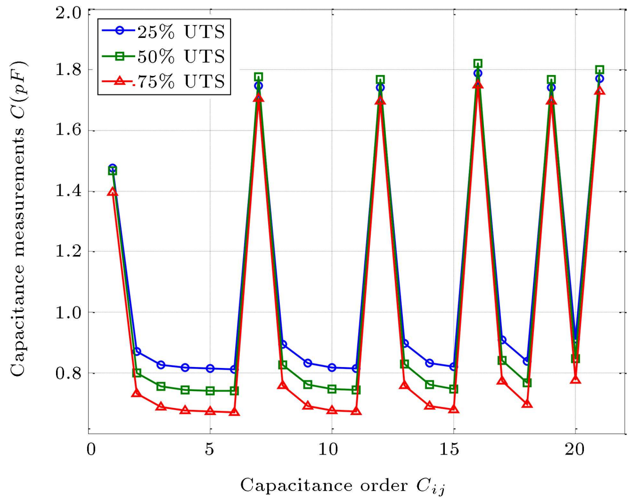

Figure 8. Effect of level of Tensile Creep (TC) ($\%\sigma_c$) on capacitance values of electrodes (pF).

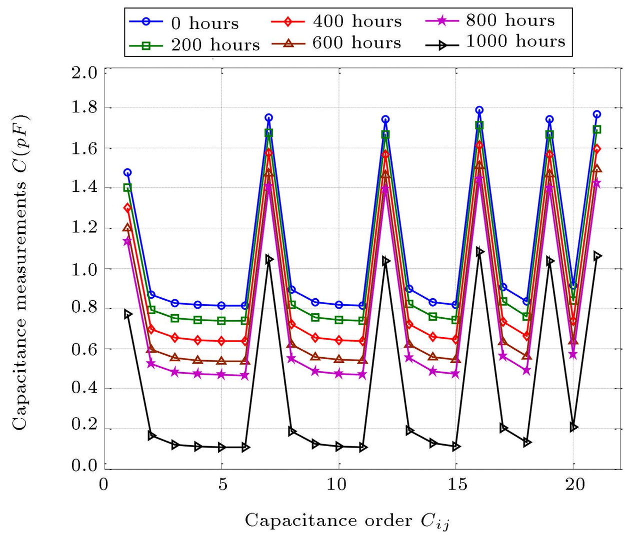

Figure 9. Effect of Creep Time (CT) on capacitance values of electrodes (pF).

The corresponding reductions in modulus over the 1000-hour period ranged from a 20% reduction over 1000 hours at 25% UTS to a 68% reduction for 1000 hours at 75% UTS.

The exponential formula (9) to fit the FE results of TCC ($S(t)$) proved satisfactory by allocating applicable values to the Correlation Factor (CF) that were very close to unity. The values of four constants a, b, k, and h at $\theta = 25$°C are shown in Table 3.

$$S(t) = ae^{bt} + ke^{ht}. \tag{9}$$

Figures 8 and 9 show the 21 capacitance measurements (C_{ij}) from 3D ANSYS model at different levels of TC ($\%\sigma_c$) and CT, respectively.

As shown in Figures 8 and 9, it can be observed that the effects of TC and CT on the capacitance

Table 3. Creep compliance constants a, b, k, and h for Tensil Creep (TC) ($\%\sigma_c$).

Tensile creep ($\%\sigma_c$) level	C.F	$a \times 10^{-11}$	$b \times 10^{-7}$	$k \times 10^{-13}$	h
**15%	0.9945	3.281	–4.365	–3.965	–0.008062
*25%	0.9974	3.079	–4.082	–4.236	–0.007138
**35%	0.9947	2.554	–4.064	–4.938	–0.007641
*50%	0.9958	2.282	–3.906	–5.095	–0.008072
**60%	0.9936	2.065	–4.429	–5.465	–0.007822
*75%	0.9963	1.891	–4.733	–6.514	–0.007443
**85%	0.934	1.645	–4.779	–6.967	–0.007336
Avg.			–4.3368		–0.007644
S.D			0.33831		0.000360

Remark: *FEM data, and **FFNN expected data.

measurement (C_{ij}) distributions are introduced and a reduction in capacitance values between electrodes occurs. This reduction depends on the level of TC ($\%\sigma_c$) and CT. Following an increase in the level of TC ($\%\sigma_c$) and CT, the capacitance values are reduced.

4.3. FFNN design for ECS to study the LTTC behavior

FFNN is shown in Figure 10. The Neural Network (NN) configuration in this case is $\{7[39 \quad 2]_2 1\}$, the first layer has tan-sigmoid neurons, and the activation function of the second layer is purely linear. The FFNN is trained in order to predict TCC ($S(t)$) by measuring values of $\%\sigma_c$, CT, θ in the input layer. First, the FFNN structure was applied to training the data of EPC at normal temperature ($\theta = 25°$C). Figure 11 shows the difference between the FE data and the FFNN predicted data (TCC) at $\theta = 25°$C at levels of TC $\%\sigma_c$ equal to 25% and 75%. According to Figure 11 containing the NN results, the high accuracy of prediction in this case study can be observed. Figure 12 represents the difference between the FE data and the FFNN expected data at ($\theta = 25°$C) at levels of TC $\%\sigma_c$ equal to 50%. It is noted that FFNN results are in agreement with the FE data.

Table 4 shows the values of MSE (see Eq. (8)) between the FE and FFNN predicted and expected results at ($\theta = 25°$C) in order to determine the best performance of the present network.

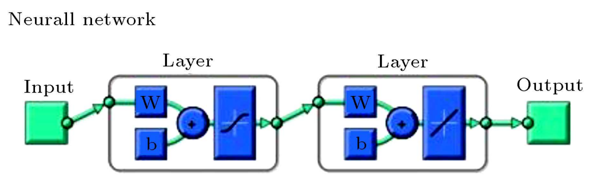

Figure 10. Schematic illustration of Feed-Formal Neural Network (FFNN) design for the present study with input data Tensil Creep (TC) ($\%\sigma_c$), Creep Time (CT), θ.

4.4. Utilizing FFNN for predicting non-FE data

The main objective of ANN design is to predict non-FE data. In this section, the suggested FFNN is used to predict some non-FE data that have been

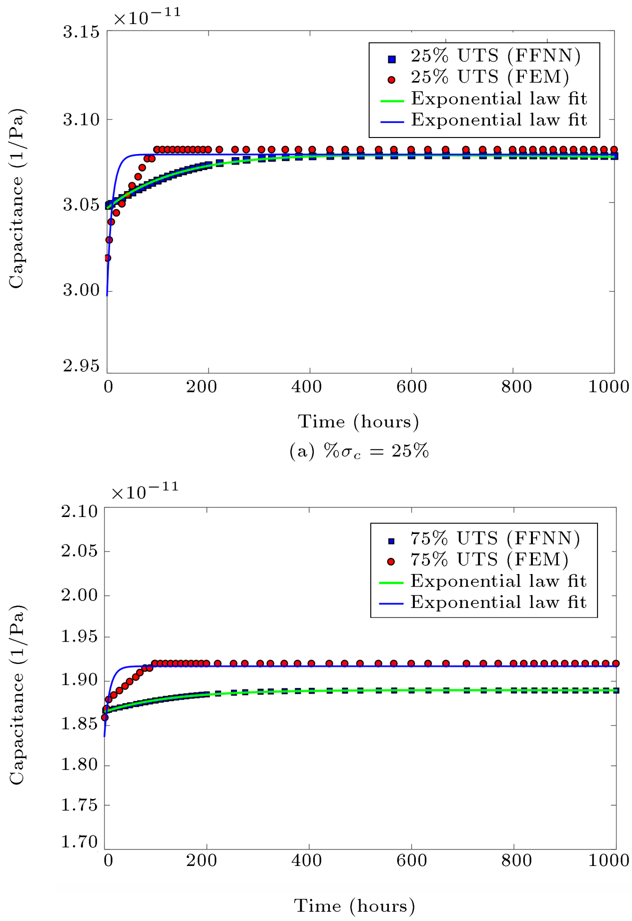

(a) $\%\sigma_c = 25\%$

(b) $\%\sigma_c = 75\%$

Figure 11. Comparison between the Finite Element (FE) data and Feed-Formal Neural Network (FFNN) predicted data at $\theta = 25°$C.

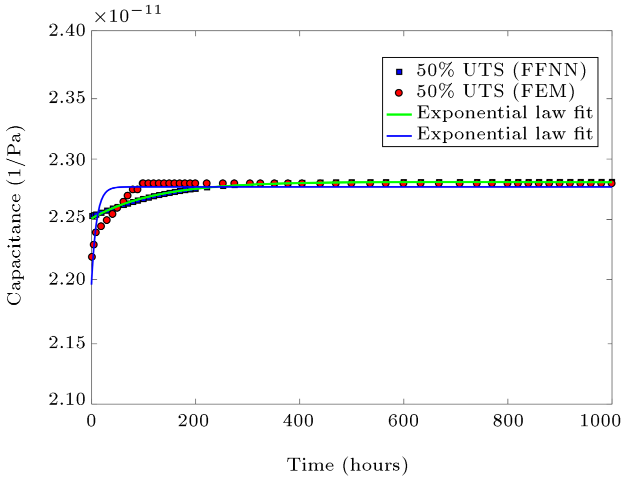

Figure 12. Comparison between the Finit Element (FE) data and Feed-Formal Neural Network (FFNN) Expected data for Tensil Creep (TC) $(\%\sigma_c)$=50% at $\theta = 25°$C.

Table 4. Mean Square Error (MSE) values.

$\theta = 25°$C		
Data	**Level of tensile creep, $\%\sigma_c$**	**MSE**
Predicted	25%	8.4916 e-27
	75%	9.7817e-26
Expected	50%	6.5020 e-27

excluded from the previous FE evaluation. FFNN is selected to be used for four cases where the level of TC $(\%\sigma_c)$ equals (15%, 35%, 60%, and 85%) for all the potential differences E_{i-j}. The previous three parameters, i.e., $\%\sigma_c$, CT, θ, are the input vectors for ANN, while the output is the signal vector for TCC $(S(t))$. Figure 13 shows the FFNN predicted results of the non-FE TCC $(S(t))$ in the BFRP laminated composite plate. The MSE of non-FE result is 2.0210E-26, 7.4194E-26, 3.1755E-26, and 1.7749E-25 for levels of TC $(\%\sigma_c)$ equal to 15%, 35%, 60%, and 85%, respectively. All of the predicted FFNN data are plotted on the diagonal line in Figure 13. Based on these results, FFNN provides good predictions about non-FE data, even about the extrapolation of LTTC behavior in the BFRP laminated composite plate.

The application of the exponential formula $S(t) = ae^{bt} + ke^{ht}$ has proved its viability by achieving acceptable values of the CF that are very close to unity. The results shown in Table 3 indicate that the proposed ANN is applied to the prediction of non-FE data.

4.5. The effect of TC $(\%\sigma_c)$ level percentage

The analysis of the values of four constants, i.e., a, b, k, and h, including the variation of TC level $(\%\sigma_c)$, TCC $(S(t))$, and CT, as documented in Table 3, led to the following results:

1. At all TC levels $(\%\sigma_c)$, the tendency curve of TCC $(S(t))$ against CT at the TC level 15% has the highest TCC. The tendency curve at the TC level 85% has the lowest TCC, while the values of the other curves at the remaining TC levels range between the above two percentages with descending orders from 25% to 75%. Thus, it can be concluded that the difference between compliance values results from fluctuations in the modulus of the composite material over the CT. The corresponding reductions in modulus over 1000 hours period ranged from a 16% reduction over 1000 hours at 15% UTS to a 78% reduction for 1000 hours at 85% UTS;

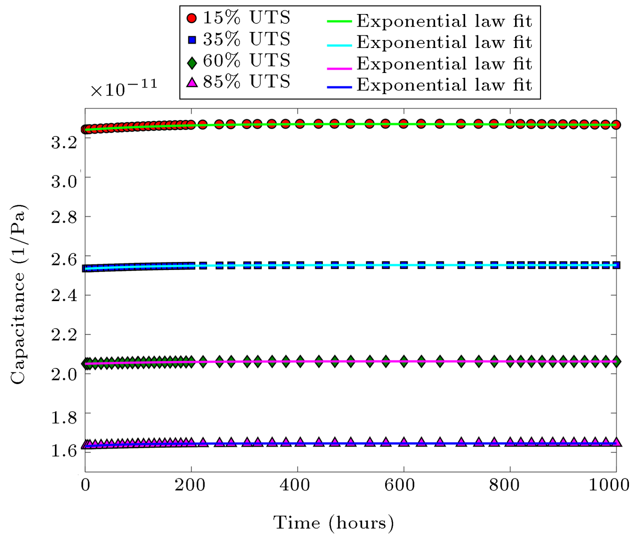

Figure 13. Expected data of Tensil Creep Compliance (TCC) $(S(t))$ at four levels of Tensil Creep (TC) $(\%\sigma_c)$ including 15, 35%, 60%, and 85% at $\theta = 25°$C.

2. The values of the constants (a and k) were found to be dependent on the TC level $(\%\sigma_c)$ for TCC $(S(t))$. As the TC level increases, the absolute value of (a and k) decreases, i.e., the TCC increases;

3. The values of the constants (b and h) at all TC levels $(\%\sigma_c)$ are negligible and may be considered constant. The average value (Avg.) of constants (b and h) was calculated and considered to be used at any TC level $(\%\sigma_c)$, as the corresponding Standard Deviation (SD) was found to have acceptable values, as shown in Table 3.

5. Conclusions

In the present study, an Electrical Potential Change (EPC) technique was adopted as an expert system for monitoring the Long-Term Tensile Creep (LTTC) behavior at different levels of TC $(\%\sigma_c)$ to improve detection efforts in order to study the LTTC behavior. The application of the proposed technique lowers the cost and reduces the time duration of the Finit Element

(FE) analysis to a minimum with higher accuracy. The results obtained are given below:

1. Electric potential difference due to LTTC at different Tensile Creep (TC) levels ($\%\sigma_c$) could be measured with multiple electrodes mounted on the outer surface of a Basalt Fiber-Reinforced Polymer (BFRP) plate;
2. The FE results showed good convergence with Feed-Forward Neural Network (FFNN) output results. This verified the accuracy and reliability of the proposed method, as shown in Table 4 and Figures 11 and 12;
3. Artificial Neural Networks (ANNs) could be employed as a method for simulating the Electrical Capacitance Sensor (ECS) from non-FE data of Tensil Creep Compliance (TCC) ($S(t)$) at TC levels ($\%\sigma_c$) equal to 15%, 35%, 60%, and 85%;
4. At all TC ($\%\sigma_c$) levels, the tendency curve of TCC ($S(t)$) against CT at the TC level (15%) had the highest TCC. The tendency curve at the TC level (85%) had the lowest TCC, while the other curves at the remaining TC levels fell in between 15%–85%, with descending order from 25% to 75%. It can be concluded that the difference between compliance values results from fluctuations in the modulus of the composite material over the CT. The corresponding reductions in modulus over a 1000-hour period ranged from a 16% reduction over 1000 hours at 15% UTS to a 78% reduction for 1000 hours at 85% UTS;
5. The exponential formula $S(t) = ae^{bt} + ke^{ht}$ proved its viability for the present study. It was found that the deviation of the constants (b and h) at different TC levels ($\%\sigma_c$) and TCC (S(t)) was negligible, which might be considered to be constant;
6. The values of the constants (a and k) were found to be dependent on the TC level ($\%\sigma_c$) and the TCC ($S(t)$) with high Correlation Factor (CF). As the TC level increased, the absolute value of (a and k) decreased, i.e., the TCC increased;
7. Finally, it can be concluded that the proposed approach provides a better understanding of the LTTC behavior at different TC levels ($\%\sigma_c$).

Acknowledgment

Collaboration of the second author with the research reported in this paper was made possible due to a release time funding from Donald E. Bently Center for Engineering Innovation, Mechanical Engineering, Cal Poly, San Luis Obispo. In addition, the second author acknowledges the support provided as a distinguished visiting professor, provided by Southeast University and the International Institute for Urban Systems Engineering for a short period of time.

References

1. Zhao, Y., Noori, M., Altabey, W.A., and Seyed, B.B. "Mode shape based damage identification for a reinforced concrete beam using wavelet coefficient differences and multi-resolution analysis", *J. Structural Control & Health Monitoring*, **25**(1), e2041 (2018). https://doi.org/10.1002/stc.2041
2. Zhao, Y., Noori, M., and Altabey, W.A. "Damage detection for a beam under transient excitation via three different algorithms", *J. Structural Engineering and Mechanics*, **64**(6), pp. 803–817 (2017). https://doi.org/10.12989/sem.2017.64.6.803
3. Zhao, Y., Noori, M., Altabey, W.A., and Awad, T. "A comparison of three different methods for the identification of hysterically degrading structures using BWBN model", *J. Front. Built Environ*, **4**, 80 (2019). DOI: 10.3389/fbuil.2018.00080
4. Altabey, W.A. and Noori, M. "An extensive overview of lamb wave technique for detecting fatigue damage in composite structures", *J. Industrial and Systems Engineering*, **2**(1), pp.1–20 (2017).
5. Altabey, W.A. "An exact solution for mechanical behavior of BFRP nano-thin films embedded in NEMS", *J. Advances in Nano Research*, **5**(4), pp. 337–357 (2017). https://doi.org/10.12989/anr.2017.5.4.337
6. Altabey, W. A. "A study on thermo-mechanical behavior of MCD through bulge test analysis", *J. Advances in Computational Design*, **2**(2), pp. 107–119 (2017). https://doi.org/10.12989/acd.2017.2.2.107
7. John, J.L., Scott, W.C., Judy, S.R., Demetri, T., and Scott, H. "Compression creep rupture of an E-glass/vinyl ester composite subjected to combined mechanical and fire loading conditions", *Thesis of Doctor of Philosophy in Engineering Mechanics*, Blacksburg, Virginia (2006).
8. Kalthoff, J.F. "Characterization of the dynamic failure behaviour of a glass fiber/vinylester at different temperatures by means of instrumented Charpy impact testing", *J. Composites: Part B*, **35**, pp. 657–663 (2008).
9. Chang, P.Y., Yeh, P.C., and Yang, J.M. "Fatigue crack initiation in hybrid boron/glass/aluminum fiber metal laminates", *J. Materials Science and Engineering: A*, **496**, pp. 273–280 (2008).
10. Goertzen, W.K. and Kessler, M.R. "Creep behavior of carbon fiber/epoxy matrix composites", *J. Materials Science and Engineering: A.*, **421**, pp. 217–225 (2006).
11. Dal Maso, F. and Meziere, J. "Calcul des propriétés élastiques des tissus utilisés dans les matériaux composites", *J. Oil & Gas Science and Technology*, **53**(6), pp. 857–870 (1998).

12. Gillham, J.K., *Encyclopedia of Polymer Science and Engineering*, 2nd Ed., John Wiley, New York, pp. 400–425 (1986).

13. Barrere, C. and Dal Maso, F. "Résines époxy réticulées par des polyamines: structure et proprieties", *J. Oil & Gas Science and Technology*, **52**(3), pp. 317–335 (1997).

14. ACI 440.4R-04 *Prestressing Concrete Structures with FRP Tendons*, American Concrete Institute, ISBN: 9780870311666 (2004).

15. Zhao, Y., Noori, M., Altabey, W.A. and Naiwei, L. "Reliability evaluation of a laminate composite plate under distributed pressure using a hybrid response surface method", Int. *J. Reliability, Quality and Safety Engineering*, **24**(3), 1750013 (2017). http://dx.doi.org/10.1142/S0218539317500139

16. Zhao, Y., Noori, M., Altabey, W.A., Ramin, G., and Zhishen, W. "A fatigue damage model for FRP composite laminate systems based on stiffness reduction", *J. Structural Durability and Health Monitoring*, **13**(1), pp. 85–103 (2019). http://dx.doi.org/10.32604/sdhm.2019.04695

17. Altabey, W.A. and Noori, M. "Fatigue life prediction for carbon fibre/epoxy laminate composites under spectrum loading using two different neural network architectures", Int. *J. Sustainable Materials and Structural Systems (IJSMSS)*, **3**(1), pp. 53–78 (2017). http://dx.doi.org/10.1504/IJSMSS.2017.10013394

18. Staszewski, W.J., Boller, C., and Tomlinson, G.R., *Health Monitoring of Aerospace Structures: Smart Sensor Technologies and Signal Processing*, Chichester (England): John Wiley and Sons Ltd. (2004).

19. Noori, M., Wang, H., Altabey, W.A. and Silik, A.I.H. "A modified wavelet energy rate based damage identification method for steel bridges", *J. Scientia Iranica, Transactions B: Mechanical Engineering*, **25**(6), pp. 3210–3230 (2018). https://doi.org/10.24200/sci.2018.20736

20. Tran, H., Noori, M., Altabey, W.A., and Wu, X. "Fault diagnosis of rotating machinery using wavelet-based feature extraction and support vector machine classifier", *J. High Speed Mach.*, **3**, pp. 23–41 (2017). http://dx.doi.org/10.1515/hsm-2017-0003

21. Altabey, W.A. "Free vibration of basalt Fiber Reinforced Polymer (FRP) laminated variable thickness plates with intermediate elastic support using finite strip transition matrix (FSTM) method", *J. Vibroengineering*, **19**(4), pp. 2873–2885 (2017). https://doi.org/10.21595/jve.2017.18154

22. Altabey, W.A. "Prediction of natural frequency of basalt fiber reinforced polymer (FRP) laminated variable thickness plates with intermediate elastic support using artificial neural networks (ANNs) method", *J. Vibroengineering*, **19**(5), pp. 3668–3678 (2017). https://doi.org/10.21595/jve.2017.18209

23. Altabey, W.A. "High performance estimations of natural frequency of basalt FRP laminated plates with intermediate elastic support using response surfaces method", *J. Vibroengineering*, **20**(2), pp. 1099–1107 (2018). https://doi.org/10.21595/jve.2017.18456

24. Altabey, W.A. "Vibration analysis of laminated composite variable thickness plate using finite strip transition matrix technique", In *MATLAB Verifications MATLAB-Particular for Engineer*; Kelly, B., Ed.; InTech, USA, **21**, pp. 583–620 . ISBN 980-953-307-1128-8 (2014). https://doi.org/10.5772/57384

25. Ghannadi, P., Kourehli, S.S., Noori, M., and Altabey, W.A. "Efficiency of grey wolf optimization algorithm for damage detection of skeletal structures via expanded mode shapes", *J. Advances in Structural Engineering*, First published online, 2 June (2020). https://doi.org/10.1177/1369433220921000

26. Lee, D.C., Lee, J.J., and Yun, S.J. "The mechanical characteristics of smart composite structures with embedded optical fiber sensors", *J. Composite Structure*, **32**, pp. 39–50 (1995).

27. Seo, D.C. and Lee, J.J. "Effect of embedded optical fiber sensors on transverse crack spacing of smart composite structures", *J. Composite Structure*, **32**, pp. 51–58 (1995).

28. Yang, W.Q., Stott, A.L., Beck, M.S., and Xie, C.G. "Development of capacitance tomographic imaging systems for oil pipeline measurements", *J. Review of Scientific Instruments*, **66**(8), pp. 4326–4332 (1995).

29. Yang, W.Q., Beck, M.S., and Byars, M. "Electrical capacitance tomography-from design to applications", *J. Measurement & Control*, **28**(9), pp. 261–266 (1995b).

30. Li, H. and Huang, Z. *Special Measurement Technology and Application*, Zhejiang University Press, Hangzhou (2000).

31. Mohamad, E.J., Rahim, R.A., Leow, P.L., Fazalul, Rahiman, M.H., Marwah, O.M.F., Nor Ayob, N.M., Rahim, H.A., and Mohd Yunus, F.R. "An introduction of two differential excitation potentials technique in electrical capacitance tomography", *J. Sensors and Actuators A.*, **180**, pp. 1–10 (2012).

32. Zhang, W., Wang, C., Yang, W., and Wang, C. "Application of electrical capacitance tomography in particulate process measurement-A review", *J. Advanced Powder Technology*, **25**, pp. 174–188 (2014).

33. Wajman, R., Fiderek, P., Fidos, H., Jaworski, T., Nowakowski, J., Sankowski, D., and Banasiak, R. "Metrological evaluation of a 3D electrical capacitance tomography measurement system for two-phase flow fraction determination", *J. Measurement Science and Technology*, **24**, 065302 (2013). https://doi.org/10.1088/0957-0233/24/6/065302

34. Zhao, Y., Noori, M., Altabey, W.A., and Zhishen, W. "Fatigue damage identification for composite pipeline systems using electrical capacitance sensors", *J. Smart Material Structures*, **27**(8), 085023 (2018). https://doi.org/10.1088/1361-665x/aacc99

35. Zhao, Y., Noori, M., Altabey, W.A., Ghiasi, R., and Zhishen, W. "Deep learning-based damage, load and support identification for a composite pipeline by extracting modal macro strains from dynamic excitations", *J. Applied Sciences*, **8**(12), 2564 (2018). https://doi.org/10.3390/app8122564

36. Altabey, W.A. and Noori, M. "Detection of fatigue crack in basalt FRP laminate composite pipe using electrical potential change method", *J. Physics: Conference Series*, **842**, 012079 (2017). https://doi.org/10.1088/1742-6596/842/1/012079

37. Altabey, W.A. "Delamination evaluation on basalt FRP composite pipe by electrical potential change", *J. Advances in Aircraft and Spacecraft Science*, **4**(5), pp. 515–528 (2017). https://doi.org/10.12989/aas.2017.4.5.515

38. Altabey, W.A. "EPC method for delamination assessment of basalt FRP pipe: Electrodes number effect", *J. Structural Monitoring and Maintenance*, **4**(1), pp. 69–84 (2017). https://doi.org/10.12989/smm.2017.4.1.069

39. Altabey, W.A. and Noori, M. "Monitoring the water absorption in GFRE pipes via an electrical capacitance sensors", *J. Advances in Aircraft and Spacecraft Science*, **5**(4), pp. 499–513 (2018). https://doi.org/10.12989/aas.2018.5.4.499.

40. Altabey, W.A., Noori, M., Alarjani, A., and Zhao, Y. "Nano-delamination monitoring of BFRP nanopipes of electrical potential change with ANNs", *J. Advances in Nano Research*, **9**(1), pp. 1–13 (2020). http://dx.doi.org/10.12989/anr.2020.9.1.001

41. Fasching, G.E. and Smith, N.S., *High Resolution Capacitance Imaging System*, US Dept. Energy, **37**, DOE/METC-88/4083 (1988).

42. Fasching, G.E. and Smith, N.S. "A capacitive system for 3-dimensional imaging of fluidized-beds", *J. Rev. Sci. Instr.*, **62**, pp. 2243–2251 (1991).

43. Huang, S.M., Plaskowski, A.B., Xie, C.G., and Beck, M.S. "Tomographic imaging of two-flow component flow using capacitance sensor", *J. Phys. E: Sci. Instrum.*, **22**, pp. 173–177 (1989).

44. Jaworski, A.J. and Bolton, G.T. "The design of an electrical capacitance tomography sensor for use with media of high dielectric permittivity", *J. Measurement Science and Technology*, **11**(6), pp. 743–757 (2000).

45. Pei, T. and Wang, W. "Simulation analysis of sensitivity for electrical capacitance tomography", in *Proceedings of Ninth International Conference on Electronic Measurement & Instruments (ICEMI 2009)*, Beijing, China (2009).

46. Altabey, W.A. "Effect of pipeline filling material on electrical capacitance tomography", In *Proceedings of the International Postgraduate Conference on Engineering (IPCE 2010)*, Perlis, Malaysia (2010).

47. Asencio, K., Bramer-Escamilla, W., Gutiérrez, G., and Sánchez, I. "Electrical capacitance sensor array to measure density profiles of a vibrated granular bed", *J. Powder Technology*, **270**, pp. 10–19 (2015).

48. Sardeshpande, M.V., Harinarayan, S., and Ranade, V.V. "Void fraction measurement using electrical capacitance tomography and high speed photography", *J. Chemical Engineering Research and Design*, **9**(4), pp. 1–11 (2015).

49. Mohamad, E.J., Rahim, R.A., Rahiman, M.H.F., Ameran, H.L.M., Muji, S.Z.M., and Marwah, O.M.F. "Measurement and analysis of water/oil multiphase flow using electrical capacitance tomography sensor", *J. Flow Measurement and Instrumentation*, **47**, pp. 62–70 (2016).

50. Altabey, W.A. "Detecting and predicting the crude oil type inside composite pipes using ECS and ANN", *J. Structural Monitoring and Maintenance*, **3**(4), pp. 377–393 (2016). http://dx.doi.org/10.12989/smm.2016.3.4.377

51. Wang, B., Tan, W., Huang, Z., Ji, H., and Li, H. "Image reconstruction algorithm for capacitively coupled electrical resistance tomography", *J. Flow Measurement and Instrumentation*, **40**, pp. 216–222 (2014). https://doi.org/10.1016/j.flowmeasinst.2014.07.006

52. Chandrasekera, T.C., Li, Y., Moody, D., Schnellmann, M.A., Dennis, J.S., and Holland, D.J. "Measurement of bubble sizes in fluidised beds using electrical capacitance tomography", *J. Chemical Engineering Science*, **126**, pp. 679–87 (2015). https://doi.org/10.1016/j.ces.2015.01.011

53. Daoye, Y., Bin, Z., Chuanlong, X., Guanghua T., and Shimin, W. "Effect of pipeline thickness on electrical capacitance tomography", In *Proceedings of the 6th International Symposium on Measurement Techniques for Multiphase Flows, J. Physics: Conference Series*, **147**, pp. 1–13 (2009).

54. Altabey, W.A. "FE and ANN model of ECS to simulate the pipelines suffer from internal corrosion", *J. Structural Monitoring and Maintenance*, **3**(3), pp. 297–314 (2016). http://dx.doi.org/10.12989/smm.2016.3.3.297

55. Altabey, W.A. "The thermal effect on electrical capacitance sensor for two-phase flow monitoring", *J. Structural Monitoring and Maintenance*, **3**(4), pp. 335–347 (2016). http://dx.doi.org/10.12989/smm.2016.3.4.335

56. ANSYS Low-Frequency Electromagnetic analysis Guide, The Electrostatic Module in the Electromagnetic subsection of ANSYS, ANSYS, Inc. Southpointe 275 Technology Drive Canonsburg, PA 15317, Published in the USA (2015).

57. Al-Tabey, W.A. "Finite element analysis in mechanical design using ANSYS", *Finite Element Analysis (FEA) Hand Book For Mechanical Engineers With ANSYS Tutorials*, LAP Lambert Academic Publishing, Germany (2012). ISBN 978-3-8454-0479-0.
58. Altabey, W.A., Mohammad, N., and Wang, L., *Using ANSYS for Finite Element Analysis: A Tutorial for Engineers*, **I**; Momentum Press, New York, NY, USA (2018). ISBN 978-1-94708-321-9.
59. Altabey, W.A., Mohammad, N., and Wang, L., *Using ANSYS for Finite Element Analysis: Dynamic, Probabilistic, Design and Heat, Transfer Analysis*, **II**, Momentum Press: New York, NY, USA (2018). ISBN 978-1-94708-323-3.
60. Jin-Gang, F., Dong-Mei, Z., Wan-Cheng, Z., and Fa, L. "Anisotropic dielectric properties of short carbon fiber composites", *J. Inorganic Materials*, **27**(11), pp. 1223–1227 (2012). http://dx.doi.org/10.3724/SP.J.1077.2012.12364
61. Angelidis, N., Khemiri, N., and Irving, P.E. "Experimental and finite element study of the electrical potential technique for damage detection in CFRP laminates", *J. Smart Materials and Structures*, **14**(1), P. 147 (2004). https://doi.org/10.1088/0964-1726/14/1/014
62. Yoshiyasu, H., Takuya, Y., and Akira, T. "Through-thickness electrical conductivity of toughened CFRP laminate", *J. Composites Science and Technology*, **122**(18), pp. 67–72 (2016). https://doi.org/10.1016/j.compscitech.2015.11.018.
63. Kost, A., Altabey, W.A., Noori, M., and Awad, T. "Applying neural networks for tire pressure monitoring systems", *J. Structural Durability and Health Monitoring*, **13**(3), pp. 247–266 (2019). https://doi.org/10.32604/sdhm.2019.07025
64. Demuth, H. and Beale, M., *Neural Network Toolbox User's Guide for use with MATLAB Version 4.0*, The Math Works, Inc. (2000).
65. Skapura D., *Building Neural Networks*, ACM Press, Addison-Wesley Publishing Company, New York (1996).
66. Goertzen, W.K. and Kessler, M.R. "Creep behavior of carbon fiber/epoxy matrix composites", *J. Materials Science and Engineering A.*, **421**, pp. 217–225 (2006).
67. Lombart, V. "In-situ creep rupture fixture to characterize structural automotive polymer matrix composites", M.S. Thesis, the University of Tulsa Graduate School (2002).

Biographies

Wael A. Altabey is an Associate Professor of Mechanical Engineering, Faculty of Engineering, Alexandria University, Alexandria, Egypt. He is currently an Associate Researcher and a visiting scholar at Engineering Mechanics, in Southeast University, Nanjing, China. He was awarded a postdoctoral research certificate in 2018 from Southeast University, Nanjing, China after completing a post-doctoral research fellowship for two years under the supervision of Professor Noori in SHM and damage detection. Dr. Altabey received his PhD in 2015 in the area of fatigue of composite structures, MSc in Dynamic Systems in 2009, and BSc in Mechanical Engineering in 2004 from Mechanical Engineering Department, Faculty of Engineering, Alexandria University. For the past 5 years, his research has focused on the utilization of AI-based schemes for structural health monitoring in the research group of Professor Noori. He has published over 40 refereed papers and 10 conference papers, served as an editorial board member of two journals in his work field, and delivered over 20 invited talks.

Mohammad Noori is a Professor of Mechanical Engineering at California Polytechnic State University, San Luis Obispo, California, USA. He is also a Distinguished Visiting National Chair Professor of 1000 Talent Program at the International Institute for Urban Systems Engineering, Southeast University, China. Prior to Cal Poly, Professor Noori served as a Higgins Professor and the Head of Mechanical Engineering at Worcester Polytechnic Institute, as an RJ Reynolds Professor and the Head of Mechanical and Aerospace Engineering at NC State University, and as a co-founder and Liasion Professor of National Institute of Aerospace. He has served as the Chair of the ASME National Committee of Mechanical Engineering Department Heads as a member of numerous US-Japan cooperative research programs, sponsored by NSF, and has received the Japan Society for the Promotion of Science Fellowship. He has served as a Program Director at NSF and has held leading positions in numerous national and international scientific organizations and professional societies. Noori has carried out original research work in nonlinear random vibrations and hysteretic systems in multi-functional structures; for the past 15 years, his research has focused on the utilization of AI-based schemes for structural health monitoring. He is an ASME Fellow, has published over 200 refereed papers, and has served as an executive editor, an associate editor, an editorial board member of several journals, a technical advisor, and a board member of numerous scientific organizations and industries. He has delivered over 120 keynote and invited talks. He is an elected member of several professional honor societies.

Ali Alarjani is an Assistant Professor at Mechanical Engineering Department at Prince Sattam bin Abdulaziz University, Alkharj, KSA. In February 2018, he graduated from University of Wisconsin, Milwaukee, Wisconsin, USA. He has completed his PhD on global economy data clustering analysis. Dr. Alarjani holds a Bachelor of Science degree in Mechanical Engineering from King Fahad University for Petroleum and Minerals and Master and PhD degrees in Industrial Engineering. Dr. Alarjani's research background is in operations research field, mathematical modeling, renewable energy data clustering analysis, and machine learning prediction.

Ying Zhao is currently a postdoctoral fellow at Civil Engineering school, Southeast University, China. His research interests involve wavelet-based signal processing approach, system identification, and development of innovative SHM algorithms for industry applications.